Visualization of RIM-BP2's crane-like function in neuronal vesicle transport using FRET

Check for updates

Tianyu Gao[1,2], Wang Li[2], Shuai Shao[1,2], Zhengyao Zhang[3], Na Li[1,2], Hangyu Zhang[1,2] & Bo Liu [1,2] ✉

"The last mile" of neuronal vesicles, from being tethered by the active zone filaments to docking at the presynaptic membrane, remains unclear, which limits the deep understanding of synaptic transmission and related physiological changes. Here, we develop two molecular biosensors (BKTS and RKTS) based on fluorescence resonance energy transfer technology according to the structure of RIM-BP2. By detecting the spatial distance between the two ends of the RIM-BP2 and the presynaptic membrane separately, the spatial posture changes in RIM-BP2 are reflected to explore how vesicles are transported to the presynaptic membrane for fusion. In the process of vesicle release, RIM-BP2 in primary cortical neurons and SH-SY5Y cells rotates like a "crane" with amino terminal deviating from the presynaptic membrane while the carboxyl terminal becomes closer. Furthermore, disturbing the microfilament or enhancing cell membrane fluidity inhibits the rotation of RIM-BP2. Through mutating RIM-BP2, we find that actin filaments provide mechanical stress through RIM-BP2 amino terminal, thereby regulating vesicle transport and release. Our work identifies a purely mechanical pathway of vesicle transport, in which microfilaments power the RIM-BP2 to drag vesicles to the presynaptic membrane as a "crane" for further release.

Mechanical factors are crucial to the entire process of neuronal vesicle transport from maturation at the trans-Golgi[1] to eventual release by fusion with the presynaptic membrane. Kinesin and dynein drive the bidirectional polarized transport of mature vesicles across microtubules[2]. A stable intracellular mechanical environment is critical for this process of transport, including the orientation, length, and spacing of microtubules[3,4] as well as the dynamics of membrane stability[5,6]. Upon reaching the nerve terminal, vesicles are transported between multiple vesicle pools driven by physical (F-actin and molecular motors) and chemical (myosin ATPase[7] and Ral-GTPases[8]) factors.

The vesicle transport described above only serves as a pre-reserve[9]. Before fully docking with the presynaptic membrane as components of the readily releasable pool (RRP), vesicles remain tethered by active zone filaments and undergo activity-dependent replenishment to sustain subsequent exocytosis[10,11]. Therefore, "the last mile" of vesicle transport, wherein these abundant tethered vesicles replenish the RRP that is docked to the presynaptic membrane upon stimulation, guarantees the precise spatial and temporal coordination of vesicle release. This critical final phase is coordinately regulated by multiple biochemical factors. For instance, elevated $[Ca^{2+}]_i$ during action potentials neutralizes the negative charges in the aspartic acid residues within the C2A and C2B domains of the Synaptotagmin I[12] and affects phosphatidylinositol (4,5)-bisphosphate[13,14]. Additionally, the phosphorylation of Bassoon[15] and SEPTIN5[16] regulates vesicle docking and release in the next step by modulating the binding of Soluble NSF Attachment protein Receptor (SNARE) proteins. However, the vesicle transport in this region manifests more as a change of vesicles in physical spatial location, and an exclusive biochemical perspective falls short in providing a comprehensive understanding. The "SNARE" hypothesis, widely recognized in secretory cells, only describes the fusion after docking[17,18], and there is still an unclear gap in how vesicles are moved on the nanoscale between the RRP and presynaptic membrane prior to docking.

Notably, synapsin, which mediates vesicle mobilization from distal reserve pools, exhibits limited expression within active zone microdomains[19]. Furthermore, electron-microscopic tomography revealed a notable shortening of tethering filaments adjacent to vesicles during action potentials[20]. These filaments comprise protein aggregates localized in the active zone[21], such as the RIM/RIM-BP, which anchors Cav2 to the active zone by directly binding to its C-terminal intracellular domain[18], and interacts with Unc13[22] to

[1]Cancer Hospital of Dalian University of Technology, Shenyang, China. [2]Faculty of Medicine, Liaoning Key Lab of Integrated Circuit and Biomedical Electronic System, Dalian University of Technology, Dalian, China. [3]School of Chemical Engineering, Ocean and Life Science, Dalian University of Technology, Panjin, China. ✉e-mail: lbo@dlut.edu.cn

synchronize action potential signals[23]. Remarkably, the structural anchoring of these complexes in the active zone and their close association with the cytoskeleton make them susceptible to stress changes[24–26]. And the stress on them may be a pivotal determinant in precisely regulating vesicle dynamics. RIM-BP2, as a key structural protein within the active zone ensures the maintenance and dynamic replenishment of reserve pool[27,28], in addition to modulating the anchored state of the active zone substrate[29]. In particular, it has been hypothesized that RIM-BP2 functions similarly to a scaffold during vesicle transport[30] based on its location and its connection to the cellular stress structure[31,32], particularly the significant impairment of RRP replenishment upon its knockout[33]. Consequently, elucidating the unique contribution of RIM-BP2 in "the last mile" of vesicle transport promises insights into the spatial dynamics of vesicular transport.

Here, we developed a series of molecular biosensors targeting RIM-BP2 based on fluorescence resonance energy transfer (FRET) technology. By monitoring the energy transfer efficiency between the FRET fluorescent protein pairs, we could assess the spatial distance between the terminals of RIM-BP2 and the presynaptic membrane, providing visual insights into RIM-BP2 spatial behavior. We found that the RIM-BP2 orchestrates vesicle transport during action potentials in a purely mechanical manner by acting as a "crane" mechanism. This "crane" was driven by microfilament contraction and thereby further regulated vesicle release. Our proposed mechanical modulation offers novel perspectives on presynaptic vesicle transport, providing a comprehensive understanding of how mechanical perturbations in the extracellular environment or disruptions in self-stress structures impact neuronal transmission.

Results

Design and validation of BKTS and RKTS biosensors

Given that RIM-BP2 interacts with cellular stress structures and its deletion significantly impairs the replenishment of the RRP and precision of vesicle release, researchers have proposed that RIM-BP2 functions as a scaffold regulating vesicular trafficking. To investigate this hypothesis, we developed two genetically encoded biosensors, BKTS and RKTS. The BKTS biosensor binds to the N-terminus of RIM-BP2 via the RTLPSPP sequence derived from Bassoon, while the RKTS biosensor interacts with the C-terminus of RIM-BP2 using the RQLPQLP motif originating from RIM. Both biosensors are anchored to the phospholipid bilayer of the non-raft regions in the presynaptic membrane through a KRas motif (Fig. 1A). Additionally, we used ECFP/YPet as fluorescence protein pairs and an improved nanospring [(GPGGA)$_8$] derived from the spider silk protein flagelliform as the distance-sensitive unit (Fig. 1B). This design allows for the measurement of the piconewton stress. Changes in the distance between the N-terminus/C-terminus of RIM-BP2 and the presynaptic membrane can be detected by changes in the FRET efficiency of BKTS (N-terminus) and RKTS (C-terminus) biosensors. This detection utilizes the extremely high sensitivity of FRET technology to fluorophore separation, enabling real-time monitoring of changes in the spatial posture of RIM-BP2 in living cells.

After transfecting the constructed BKTS and RKTS biosensors into SH-SY5Y cells for 24 h, dual-channel fluorescence images (ECFP and YPet) were acquired via laser scanning confocal microscopy, confirming successful intracellular expression of the biosensors as shown in Fig. 1C and F. Electrical stimulation (10 Hz, 5 min) was applied to the cells, and captured dual channel fluorescence images before and after stimulation. Following processing to obtain YPet/ECFP FRET ratio images (Fig. 1D, E, G, H), K-means clustering was employed to categorize FRET ratio images into regions with significant ratio changes (Fig. 1D, G) and regions without changes (Fig. 1E, H), enabling subcellular localization analysis of stimulation responses. The results revealed that BKTS biosensors exhibited a significant decrease in FRET ratio at axon terminal regions (red dashed boxes, Fig. 1D) post-stimulation, while other cellular regions showed no remarkable alterations (Fig. 1E). Conversely, RKTS biosensors demonstrated a marked increase in FRET ratio at axon terminals (red dashed boxes, Fig. 1G) after stimulation, with other cellular regions showed no remarkable alterations (Fig. 1H). These findings collectively indicate that our engineered

BKTS and RKTS biosensors achieve proper intracellular expression and respond to electrical stimulation through FRET ratio changes.

To confirm that the observed FRET ratio changes originate from posture alterations of RIM-BP2, we generated three control biosensors variants by removing anchoring sequences: BTS and RTS (lacking membrane-targeting sequences, Fig. 1I, J) and KTS (lacking the RIM-BP2-binding domain, Fig. 1K). In SH-SY5Y cells, none of these control biosensors exhibited detectable FRET ratio changes following electrical stimulation. Furthermore, we designed three siRNA constructs targeting endogenous RIM-BP2 (siRIMBP2-1, 2, 3). The knockdown mediated by siRIMBP2-1 reduced RIM-BP2 expression levels to 15% (Supplementary Fig. 1A, B), with immunofluorescence confirming significantly attenuated subcellular localization signals (Supplementary Fig. 1C). Co-transfection of the biosensors with siRIMBP2-1 into SH-SY5Y cells revealed that knocking down RIM-BP2 eliminated the stimulation-induced FRET ratio responses in both BKTS and RKTS biosensors (Fig. 1L–N). Collectively, these functional validations establish that the FRET ratio changes in our biosensors specifically report conformational dynamics of RIM-BP2.

Next, we validated the spatial correspondence between FRET ratio changes and RIM-BP2-enriched regions. Applying K-means clustering to immunofluorescence images of endogenous RIM-BP2 in SH-SY5Y cells to extract RIM-BP2-enriched regions. The results showed that its localization in the synaptic terminal region was highly consistent in morphology and distribution with the regions identified by our K-means method based on changes in the FRET ratio of two biosensors during stimulation (Supplementary Fig. 2). To directly demonstrate the spatial correspondence between RIM-BP2 localization and FRET signal changes, we labeled presynaptic vesicle clusters in SH-SY5Y cells transfected with the biosensors using lipophilic FM4-64 dye. After electrical stimulation, regions exhibiting FRET ratio changes in both BKTS and RKTS biosensors precisely overlapped with sites of vesicle cluster release (Supplementary Fig. 3). Furthermore, colocalization analysis of immunofluorescence labeled RIM-BP2 and the presynaptic vesicle membrane marker Synaptophysin demonstrated significant overlap in both whole-cell distribution and axon terminal clustering patterns (Supplementary Fig. 4). This nanoscale spatial congruence among the localization of FRET signal changes, RIM-BP2, and the vesicle marker protein Synaptophysin provides compelling evidence that the observed FRET ratio alterations occur specifically at RIM-BP2-enriched sites. In summary, through functional validation and subcellular localization studies, we have conclusively demonstrated that our biosensors exhibit precise subcellular specificity and can reliably monitor changes in the spatial posture of RIM-BP2.

The stability, sensitivity, reversibility and linearity of the BKTS and RKTS biosensors were validated with the stimulation protocols shown in Fig. 2A. Under basal conditions without any stimulation, the FRET ratio of both BKTS and RKTS did not fluctuate significantly over 5 min recordings, indicating their stability in living cells (Fig. 2B, C). Application of a single suprathreshold electrical stimulation immediately induced changes in the FRET ratio of two biosensors, with complete restoration to baseline levels after stimulation (Fig. 2D, E). It indicated that the biosensors were able to respond precisely to one single action potential with sufficient sensitivity and reversibility. To further characterize stimulus-response relationships, we maintained constant field strength and pulse duration while varying stimulation frequency (2 Hz, 10 Hz, 20 Hz). Both biosensors showed frequency-dependent FRET ratio changes, and not only were there significant differences in FRET ratios among the various groups, but a strong linear relationship was also observed between frequency and FRET ratio (Fig. 2F, G).

RIM-BP2 acts as "crane" during neuronal vesicle transport

To investigate the spatial posture changes of the RIM-BP2 during vesicle release and explore its functional role in the process, we isolated cortical neurons from neonatal SD rats within 24 h after birth. After transfected with biosensors for 3 days, we induced depolarization by dropwise adding high K$^+$ solution (final K$^+$ concentration 120 mM) to trigger vesicle transport
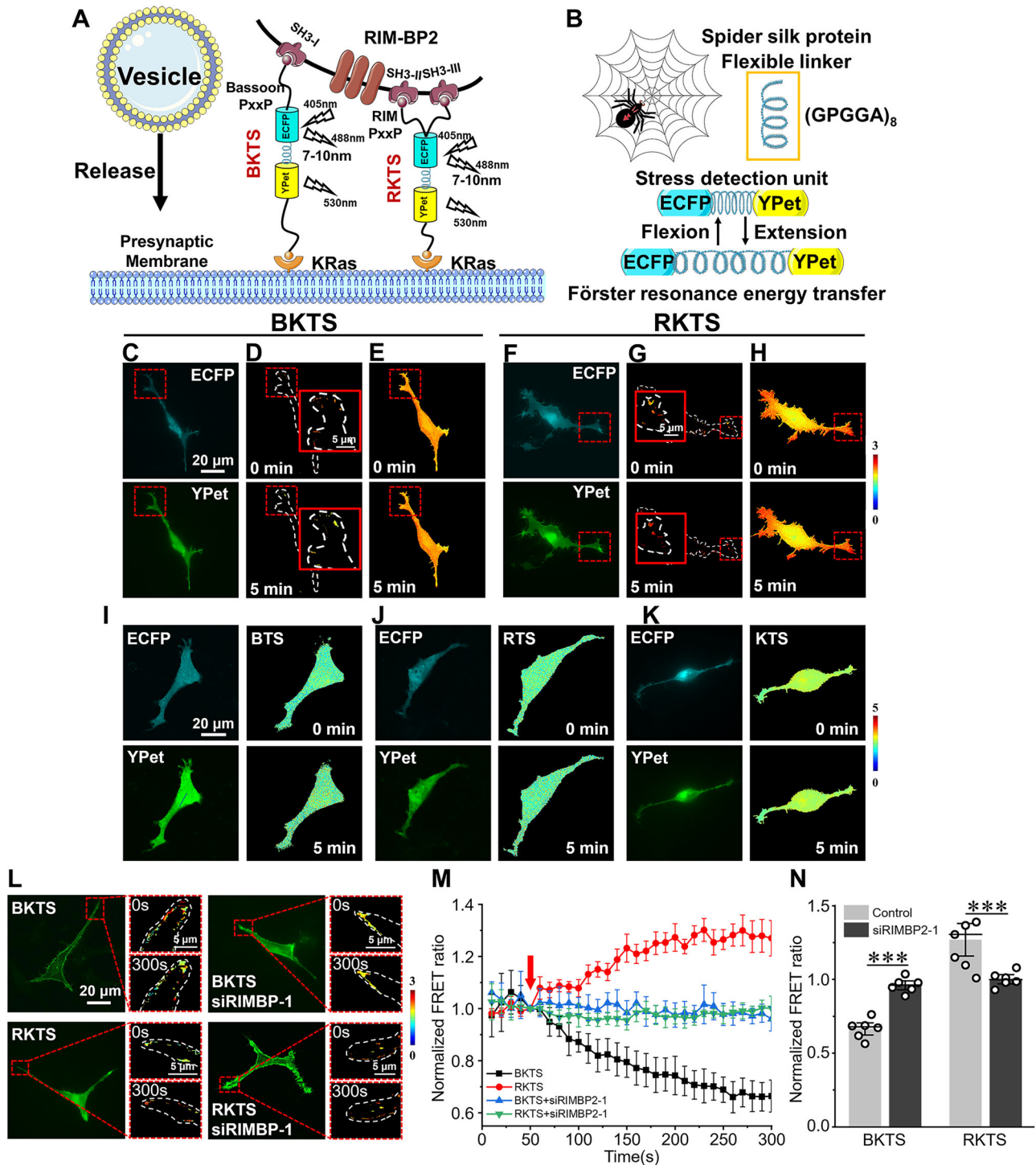
Fig. 1 | The structure, localization, and expression of RIM-BP2 molecular biosensors. A Connection modes of BKTS and RKTS biosensors to RIM-BP2 and presynaptic membrane. **B** The mechanosensing principle of the stress detection unit of biosensors. The flexible linker is selected from spider silk spring protein, and the stress detection unit is equipped with FRET fluorescent protein pair. Mechanical stretching/compression alters the distance between fluorescent proteins, enabling reflection of molecular tension through FRET efficiency changes. Fluorescence images of (**C**) BKTS and (**F**) RKTS biosensor in the 488 nm emission (ECFP) and 530 nm emission (YPet) under 405 nm excitation in SH-SY5Y cells. **D, E, G, H** FRET ratio images obtained by K-means clustering analysis after YPet/ECFP. **D, G** Depict regions with significant FRET ratio changes for the BKTS and RKTS biosensors, respectively. **E, H** Illustrate non-responsive regions for the BKTS and RKTS biosensors, respectively. **I–K** Expression of (**I**) BTS, **J** RTS, and **K** KTS control biosensors in SH-SY5Y cells, and YPet/ECFP FRET ratio images of the cells during 5 min of 10 Hz electrical stimulation, respectively. **L** YPet/ECFP FRET ratio images of BKTS and RKTS in SH-SY5Y cells under electrical stimulation after knockdown of RIM-BP2 using siRIMBP2-1. **M** Normalized FRET ratio curves and **N** statistical analysis of BKTS and RKTS before and after knocking down RIM-BP2 over time. BKTS, $n = 6$; RKTS, $n = 6$. Student's t test, ***$P < 0.001$. Data are mean ± SEM.
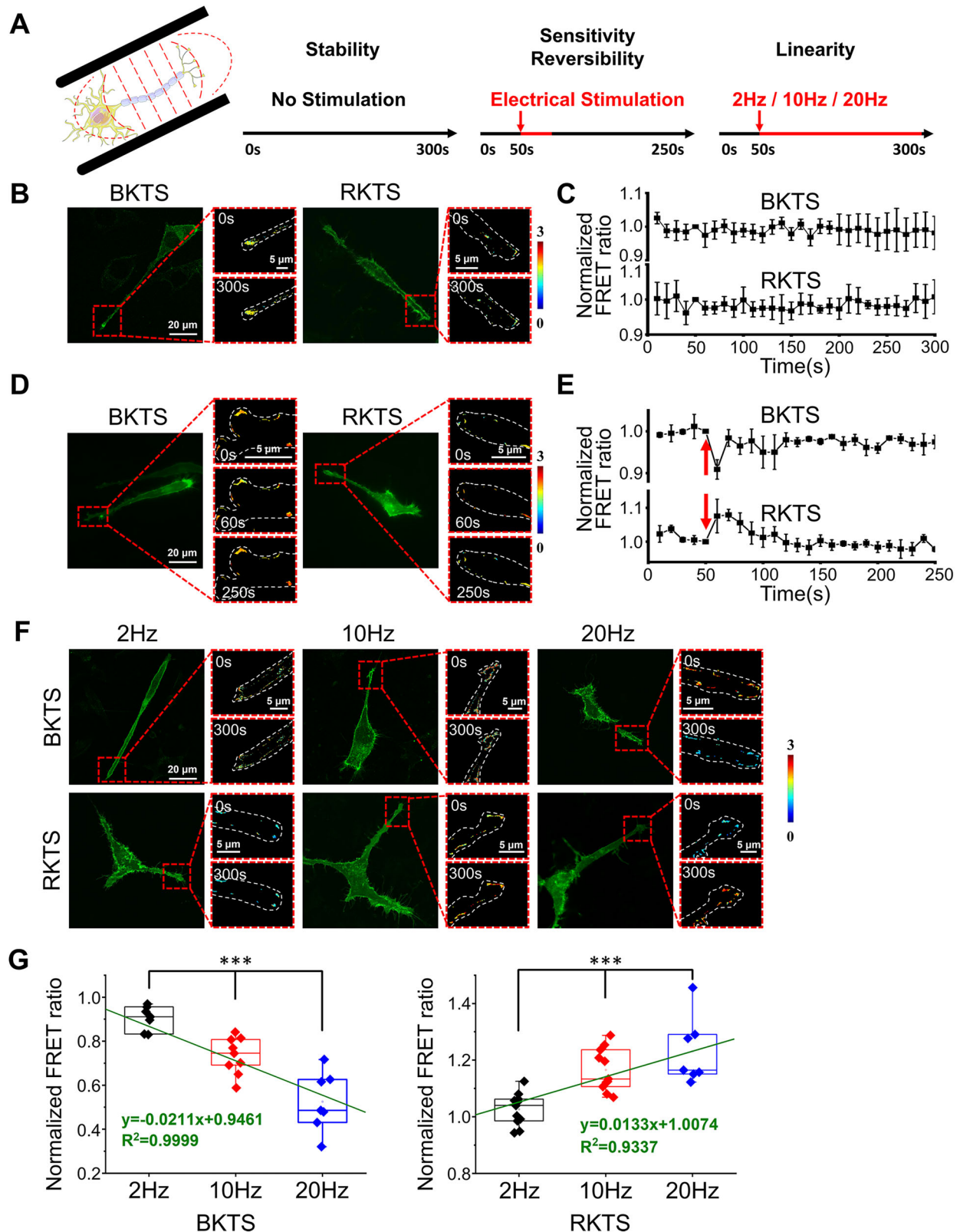
and release. This method, which inhibits the intracellular K^+ efflux to simulate neuronal excitatory conduction, has been widely applied in studies of neuronal transmission mechanisms. Under high K^+ solution stimulation, we observed a significant decrease in the FRET ratio of BKTS biosensor and a marked increase in the FRET ratio of RKTS in cortical neurons. These findings demonstrate that RIM-BP2 undergoes spatial posture changes

during vesicle release, exhibiting a mechanical characteristic akin to "crane"-like deflection. In contrast, the FRET ratios of the control biosensors BTS and RTS showed no significant changes (Fig. 3A–C).

Subsequently, we transfected SH-SY5Y cells with BKTS and RKTS and induced vesicle release using two independent methods as well: high K^+ solution stimulation and electrical stimulation. The results demonstrated

Fig. 2 | The verification of stability, sensitivity, reversibility, and linearity of biosensors in SH-SY5Y cells. A The stimulation protocol for biosensors validation. Axonal regions were aligned between bipolar electrodes. The red arrow indicates the onset of stimulation, and the red line represents the duration of the stimulation. **B, C** Verification of biosensors stability. **B** FRET channel fluorescence images of SH-SY5Y cells transfected with BKTS and RKTS, and YPet/ECFP FRET ratio images of the red dashed area processed by K-means cluster analysis at 0 s and 300 s in the resting conditions without stimulation. **C** Normalized YPet/ECFP FRET ratio of BKTS and RKTS over time at 300 s in the no stimulation conditions. BKTS, $n = 8$; RKTS, $n = 7$. D, E Verification of biosensors sensitivity and reversibility. **D** YPet/ECFP FRET ratio images of BKTS and RKTS biosensors at 0 s, 60 s, and 300 s under brief electrical stimulation. **E** Normalized YPet/ECFP FRET ratio curves of BKTS and RKTS before and after a single suprathreshold stimulation, using the FRET ratio at the last moment before stimulation as the baseline. BKTS, $n = 6$; RKTS, $n = 7$. The red arrow indicated the time point when the stimulation was applied. **F, G** Verification of biosensor linearity. **F** YPet/ECFP FRET ratio images of SH-SY5Y cells transfected with BKTS and RKTS biosensors before and after 5 min of electrical stimulation at 2 Hz, 10 Hz, and 20 Hz. **G** Linear regression analysis and statistical comparison of normalized YPet/ECFP FRET ratios for BKTS and RKTS at 300 s (Green line, fitting curve using the least squares fit). BKTS (2 Hz, $n = 7$; 10 Hz, $n = 9$; 20 Hz, $n = 7$); RKTS (2 Hz, $n = 11$; 10 Hz, $n = 11$; 20 Hz, $n = 7$). One-way ANOVA. ***$P < 0.001$. Data are mean ± SEM.

that the FRET ratio responses of BKTS and RKTS in SH-SY5Y cells were consistent with those observed in rat cortical neuron. Specifically, the FRET ratio of BKTS biosensor decreased significantly, whereas that of RKTS biosensor exhibited a significantly increase (Fig. 3D–G). In contrast, the control biosensors BTS and RTS still did not response to either stimulation (Fig. 3D–G). Notably, the magnitude of FRET ratio changes induced by high K$^+$ solution stimulation and electrical stimulation showed no statistically significant difference within the same timeframe (Fig. 3H). Using FM4-64 to label vesicle trafficking in SH-SY5Y cells, we observed that RIM-BP2 knockdown mediated by *siRIMBP2-1* significantly impaired vesicle trafficking activity (Supplementary Fig. 5). These findings collectively demonstrate that the mechanical characteristics of RIM-BP2's "crane" deflection play a critical role in regulating vesicle trafficking, and these characteristics remain conserved across neuronal cell types and stimulation modalities, with universality.

Microfilaments power the "crane" behavior to regulate vesicle transport

To investigate whether cytoskeletal drives the "crane" behavior of RIM-BP2 during vesicle release, we disrupted the structure and function of actin filament stress using cytochalasin D (CytoD) and myosin light chain kinase inhibitor (ML-7), while monitoring changes in the FRET ratio of the biosensors under electrical stimulation. Phalloidin staining showed that incubation with 1 μM CytoD for 30 min significantly disrupted the morphology of microfilaments in SH-SY5Y cells, leading to the dissociation of intact filamentous structures. In contrast, treatment with 5 μM ML-7 for 1 h did not alter the ultrastructure of microfilament (Supplementary Fig. 6). The FRET ratio of both BKTS and RKTS biosensors showed no significant response to electrical stimulation following microfilament disruption using CytoD, demonstrating significant differences compared to untreated controls with intact actin structures. Further experiments using ML-7 to block microfilament contraction without damaging the structure, revealed similar response deficits in FRET ratios, indicating that functional actin microfilament-contraction rather than mere structural integrity regulates this process. In contrast, inhibition of microtubule polymerization with 150 nM Nocodazole (NOCO) for 15 min did not impair the electrical stimulation-induced FRET ratio changes of in either BKTS or RKTS biosensors (Fig. 4A-C). Quantitative analysis confirmed no statistically significant differences in response amplitudes between NOCO-treated and control group (Fig. 4D). These findings suggest that the microfilament contraction drives the RIM-BP2 "crane" behavior, while microtubule networks appear dispensable for this regulatory mechanism.

To investigate whether the changes in RIM-BP2 caused by altered cytoskeleton dynamics affect vesicle release dynamics, we utilized the amphiphilic styryl dye FM4-64 to monitor the vesicles in SH-SY5Y cells. Prior to live-cell imaging, to eliminate any potential interference among the three fluorescence of FM4-64 and the fluorescent protein pairs of biosensors, we mixed the dye with purified stress detection unit proteins (containing ECFP and YPet fluorescent pairs). Full-spectrum scanning using an enzyme marker confirmed no spectral overlap between the excitation/emission spectra of FM4-64's red fluorescence and ECFP/YPet (Fig. 4E). FM4-64 did not alter the energy transfer of biosensors, nor did

FRET phenomena affect FM4-64 fluorescence intensity (Fig. 4F), thereby eliminating potential interference. In cellular experiments revealed that the CytoD-mediated disruption of actin filaments or ML-7-induced inhibition of actomyosin contraction significantly attenuated FM4-64-labeled vesicle release (Fig. 4G–I). In contrast, microtubules depolymerization by NOCO preserved total vesicle released capacity, but altered release kinetics (Fig. 4G–I). It might be because microtubules may regulate mechanical feedback during vesicle replenishment. This collectively demonstrates that the contraction of actin microfilaments drives the "crane" behavior of RIM-BP2, thereby regulating vesicle release.

Membrane tension affects stress transfer of "crane" behavior

The cell membrane, serving as the primary structure for sensing mechanical stimulation and initiating cellular responses, plays a pivotal role in pressure transmission and osmotic regulation. Given that vesicle release involves membrane fusion with the presynaptic membrane[34], the mechanical characteristics of the cell membrane may significantly influence the dynamics of the RIM-BP2 "crane" behavior. To investigate how membrane tension regulates the dynamic function of RIM-BP2, we employed an indirect approach by modulating static membrane tension through alterations in membrane fluidity. Using the MSS FRET biosensor[35], we confirmed the efficacy of this strategy: treatment with 0.1 mM cholesterol (CHO) for 3 h effectively reduced membrane fluidity in SH-SY5Y cells, thereby increasing static membrane tension, whereas 20 mM benzyl alcohol (BA) treatment for 15 min enhanced membrane fluidity while decreasing static tension (Fig. 5A, B). These results indicate that altering membrane tension through modulation of membrane fluidity is a feasible approach for investigating the effect of membrane tension on RIM-BP2 "crane" behavior.

We observed that upregulation of membrane tension significantly enhanced the magnitude of FRET ratio changes in both BKTS and RKTS biosensors in SH-SY5Y cells during electrical stimulation. Conversely, downregulation of membrane tension attenuated the FRET ratio response magnitude (Fig. 5C–F). It suggests that membrane tension, modulated through membrane fluidity, affects the "crane" behavior of RIM-BP2.

Amino terminal of RIM-BP2 realizes stress transfer of vesicle transport

RIM-BP2 is directly connected to vesicles via RIM-binding domain at its carboxyl terminal. Therefore, to distinguish whether the "crane" behavior represents active movement or displacement secondary to vesicle release, and to determine the specific site of action of actin filament stress, we constructed two RIM-BP2 mutants: RIM-BP-SH3 (disrupting the connection of RIM-BP2 carboxyl terminal) and RIM-BP-SH3-2 (disrupting the connection of RIM-BP2 amino terminal) (Fig. 6A). The mutants are integrated with an mCherry fluorescent tag and employ a dual-promoter expression system to achieve independent expression of the mCherry tag and the mutant gene, enabling real-time tracking of mutated cells through fluorescent signaling. Co-transfection of mCherry-tagged mutant probes and biosensors into SH-SY5Y cells demonstrated clear simultaneous excitation of three fluorescent signals (mCherry, ECFP, and FRET) within one individual SH-SY5Y cell. The presence of free mCherry did not affect the efficiency of energy transfer between FRET fluorescent protein pairs (Fig. 6B).
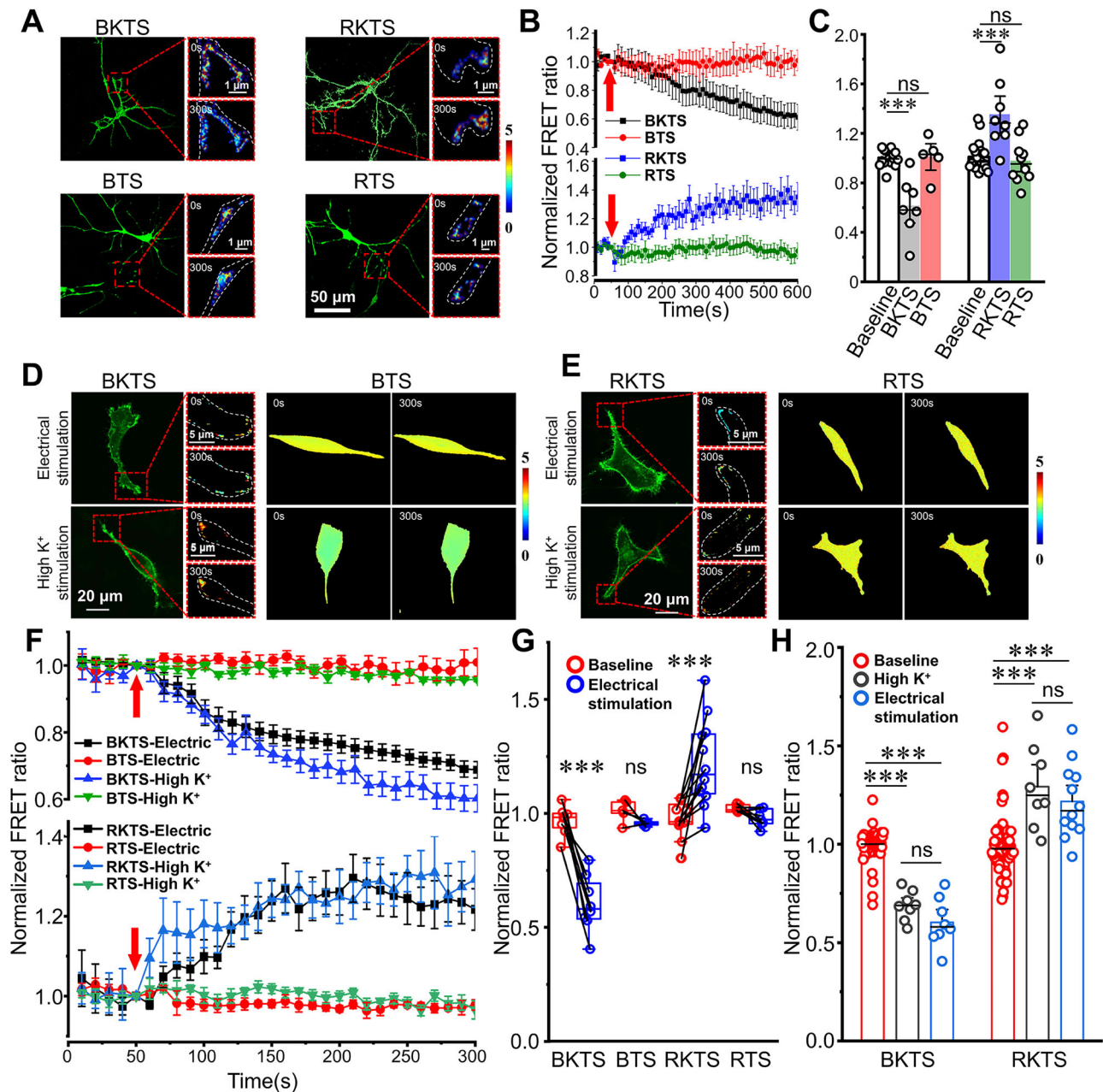
Fig. 3 | Spatial postural deflection of RIM-BP2 during action potentials in cortical neurons and SH-SY5Y cells. A Fluorescence images of BKTS, BTS, RKTS, and RTS biosensors expressed in rat cortical neurons. YPet/ECFP FRET ratio images before and after electrical stimulation are shown. **B** Trends of normalized FRET ratio for BKTS, BTS, RKTS and RTS biosensors in cortical neurons. Red arrows indicate stimulus onset. BKTS, $n = 7$; BTS, $n = 5$; RKTS, $n = 8$; RTS, $n = 10$. **C** Comparative analysis of FRET ratio values at 600 s post-stimulation, normalized to pre-stimulation baseline. **D**, **E** YPet/ECFP FRET ratio images of BKTS, BTS (**D**) and RKTS, RTS (**E**) in SH-SY5Y cells under high K+ solution stimulation and electrical stimulation. **F** Trend of YPet/ECFP FRET ratio for BKTS, BTS, RKTS and RTS under high K+ solution stimulation (BKTS, $n = 8$; BTS, $n = 6$; RKTS, $n = 8$; RTS, $n = 6$) and electrical stimulation (BKTS, $n = 8$; BTS, $n = 5$; RKTS, $n = 12$; RTS, $n = 7$). **G** FRET ratio changes of biosensors in SH-SY5Y cells during electrical stimulation. Red circles: baseline FRET ratio before stimulation; Blue circles: FRET ratio at 300 s. Black lines connect measurements of the same cell. **H** Comparative analysis of BKTS and RKTS biosensors in SH-SY5Y cells corresponding to two kinds of stimulations. Student's t test, ***$P < 0.001$, ns $P > 0.05$. Data are mean ± SEM.

In the RIM-BP-SH3 mutant cells (retaining intact amino terminal), electrical stimulation caused a significant decrease in BKTS biosensor FRET ratio, with a magnitude of change comparable to wild-type cells (Fig. 6C–E). In contrast, the RIM-BP-SH3-2 mutant cells (retaining intact carboxyl terminal) exhibited markedly attenuated RKTS biosensor FRET ratio responses (Fig. 6C–E). This indicates that the "crane" behavior of RIM-BP2 is driven by the contraction of actin filaments through the N-terminal domain of RIM-BP2. Control experiments with mCherry alone showed no

significant alteration in FM4-64-labeled vesicle release, confirming that the presence of mCherry also does not interfere with vesicle release monitoring (Fig. 6F, G). The significant reduction in vesicle release observed in both mutants (Fig. 6F, G) further confirms that RIM-BP2 "crane" behavior actively facilitates vesicle release rather than passively responding to release events. Collectively, these findings establish that actin filaments drive the "crane" behavior of RIM-BP2 through its amino terminal, thereby regulating vesicle transport and release.
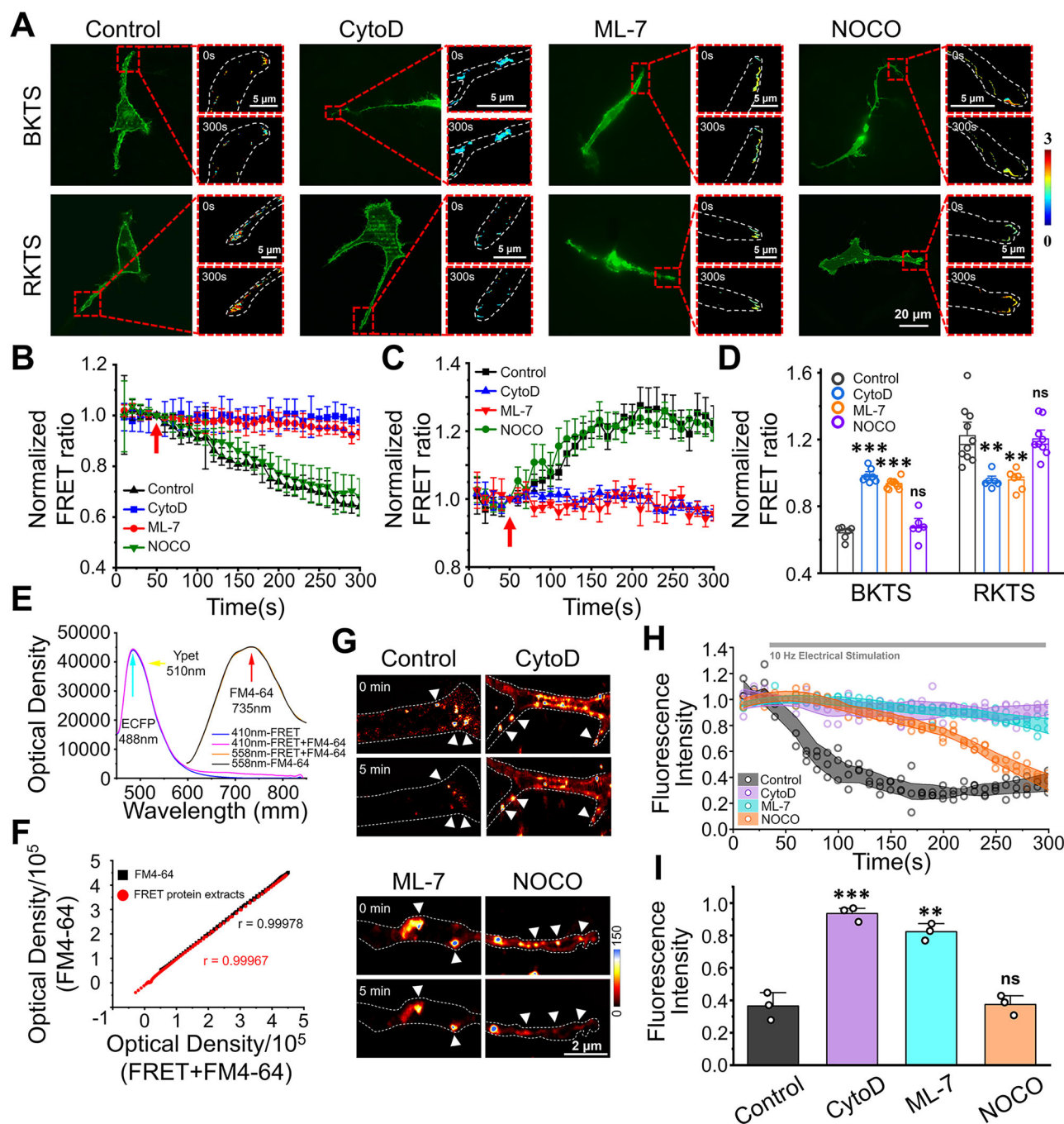
Fig. 4 | Cytoskeletal microfilaments act as a power source for the "crane" activity of RIM-BP2 in SH-SY5Y cells. A The fluorescence images and FRET ratio images of BKTS and RKTS biosensors at 0 s and 300 s during electrical stimulation under different cytoskeletal stress conditions. Pretreatment conditions: CytoD (1 μM, 30 min); ML-7 (5 μM, 1 h); NOCO (150 nM, 15 min). **B, C** Trend of YPet/ECFP FRET ratio for BKTS and RKTS biosensors under cytoskeletal perturbations. BKTS (CytoD, n = 7; ML-7, n = 9; NOCO, n = 6); RKTS (CytoD, *n* = 6; ML-7, *n* = 7; NOCO, *n* = 9). **D** Stress of RIM-BP2 "crane" activity under different cytoskeletal stress. FRET ratios were measured at 300 s post-stimulation. **E** Spectral characterizations of protein extracts of FRET fluorescent protein pair and FRET + FM4-64 mixtures. Absorbance spectra were recorded under 410 nm and 558 nm excitation.

F Correlation analysis of optical density values between individual protein extracts and mixtures. Red dots: The correlation between individual protein extracts and FRET + FM4-64 mixtures under 410 nm excitation. Black dots: The correlation between FM4-64 and FRET + FM4-64 mixtures under 558 nm excitation. Pearson test. **G** Microfilament stress modulation inhibits stimulus-evoked vesicle release. The white dashed lines outlined cells morphology, and the white triangles pointed out the FM4-64-labeled clusters. **H** The changes in fluorescence intensity of FM4-64-labeled clusters under 5 min 10 Hz stimulation following cytoskeletal perturbations. CytoD, *n* = 3; ML-7, *n* = 3; NOCO, *n* = 3. **I** Normalized fluorescence intensity values of FM4-64 bright spots at 300 s. Mann-Whitney U test, **$P < 0.01$, ***$P < 0.001$, ns $P > 0.05$. Data are mean ± SEM.

Discussion

Proteins carry intracellular mechanical stresses, regulating many physiological processes such as cell migration[36], polarity formation[37], and vesicle transfer[38,39]. Therefore, tracking the variations in stress and spatial attitude of related proteins may decipher the process behind "the last mile" of vesicle transport. First established in the 1970s as a SK-N-SH neuroblastoma subline, SH-SY5Y cells have emerged as a pivotal in vitro model for neurosecretory research, particularly due to their adrenergic properties and demonstrated capacity for norepinephrine release[40]. Their neuronal relevance is anchored in Western blot confirmation of complete presynaptic
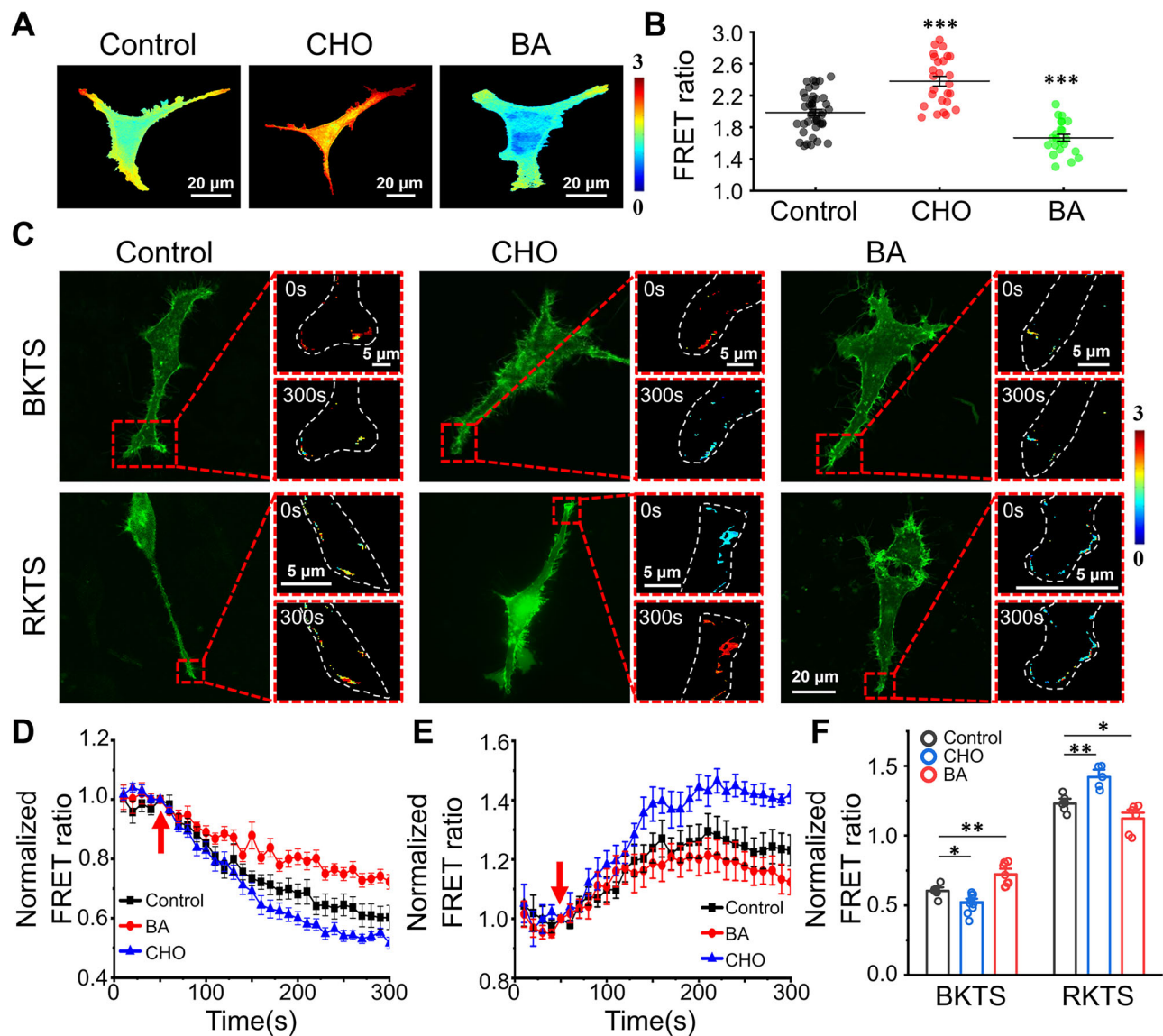
Fig. 5 | Changes in cell membrane fluidity regulate the "crane" activity of RIM-BP2 in SH-SY5Y cells. A FRET images of SH-SY5Y cells transfected with the MSS probe. **B** MSS FRET ratio values under different membrane fluidity conditions induced by CHO (0.1 mM, 3 h) and BA (20 mM, 15 min). Control, $n = 43$; CHO, $n = 26$; BA, $n = 22$. **C** The fluorescence images and YPet/ECFP FRET ratio images of BKTS and RKTS biosensors during electrical stimulation under different membrane fluidity. **D, E** Trend of YPet/ECFP FRET ratio for BKTS (**D**) and RKTS (**E**) under membrane fluidity modulation. Red arrows indicate the stimulus onset. BKTS (CHO, $n = 10$; BA, $n = 9$); RKTS (CHO, $n = 5$; BA, $n = 7$). **F** Comparative analysis of RIM-BP2 "crane" activity under different membrane fluidity. FRET ratio values were measured at 300 s. Student's *t* test. *$P < 0.05$, **$P < 0.01$, ***$P < 0.001$. Data are mean ± SEM.

protein expression—including synaptotagmin I, synaptobrevin, and SNAP-25[41]—which collectively enable vesicle trafficking and fusion mechanisms mirroring native neuronal exocytosis. Crucially, these cells preserve neuron-like transport regulation, exemplified by F-actin-dependent vesicle redistribution dynamics at terminal regions[42], providing experimentally accessible models for membrane trafficking studies. This functional fidelity extends to neurodegenerative disease modeling, with co-expression of α-Synuclein[43], amyloid precursor protein[44], and Tau[45] underpinning their widespread adoption in Parkinson's[46] and Alzheimer's disease[47] research. Therefore, SH-SY5Y cells serve as a critical in vitro model for studying neurosecretory mechanisms, providing a robust tool for investigating vesicle trafficking dynamics. This work constructed a series of specific molecular biosensors based on the FRET technique to easily measure the tiny nanoscale distance between the two ends of RIM-BP2 and the presynaptic membrane in SH-SY5Y and cortical neurons by transforming it into an amplified fluorescence energy transfer efficiency. Our results successfully observed the spatial posture alterations of RIM-BP2 during action potential,

with the amino terminus far away and the carboxyl terminal close to the presynaptic membrane, rotating like a "crane". Ultimately, our results establish a purely mechanical source of vesicle transport dynamics from the microfilament to the amino terminus of RIM-BP2.

RIM-BP2 is an important structural protein found in the active zone of the presynaptic membrane in recent years[36]. The absence of RIM-BP2 leads to the transfer of the cell matrix in the active zone from an anchored state to a free state, and leading to abnormal distribution of vesicles[29]. Its absence during the high-speed release of vesicles also reduced the rate of RRP replenishment by 400% and restricted the release rate[27]. A.G. Petzoldt[30] hypothesized that the RIM-BP2 would serve as a scaffold based on changes in the vesicle release process following its deletion. However, the minor conformational changes of proteins and the rapid process of vesicle release pose significant challenges to the spatial and temporal resolution of detection methods. Consequently, there is still a lack of direct observation and in-depth exploration of RIM-BP2 functionality.
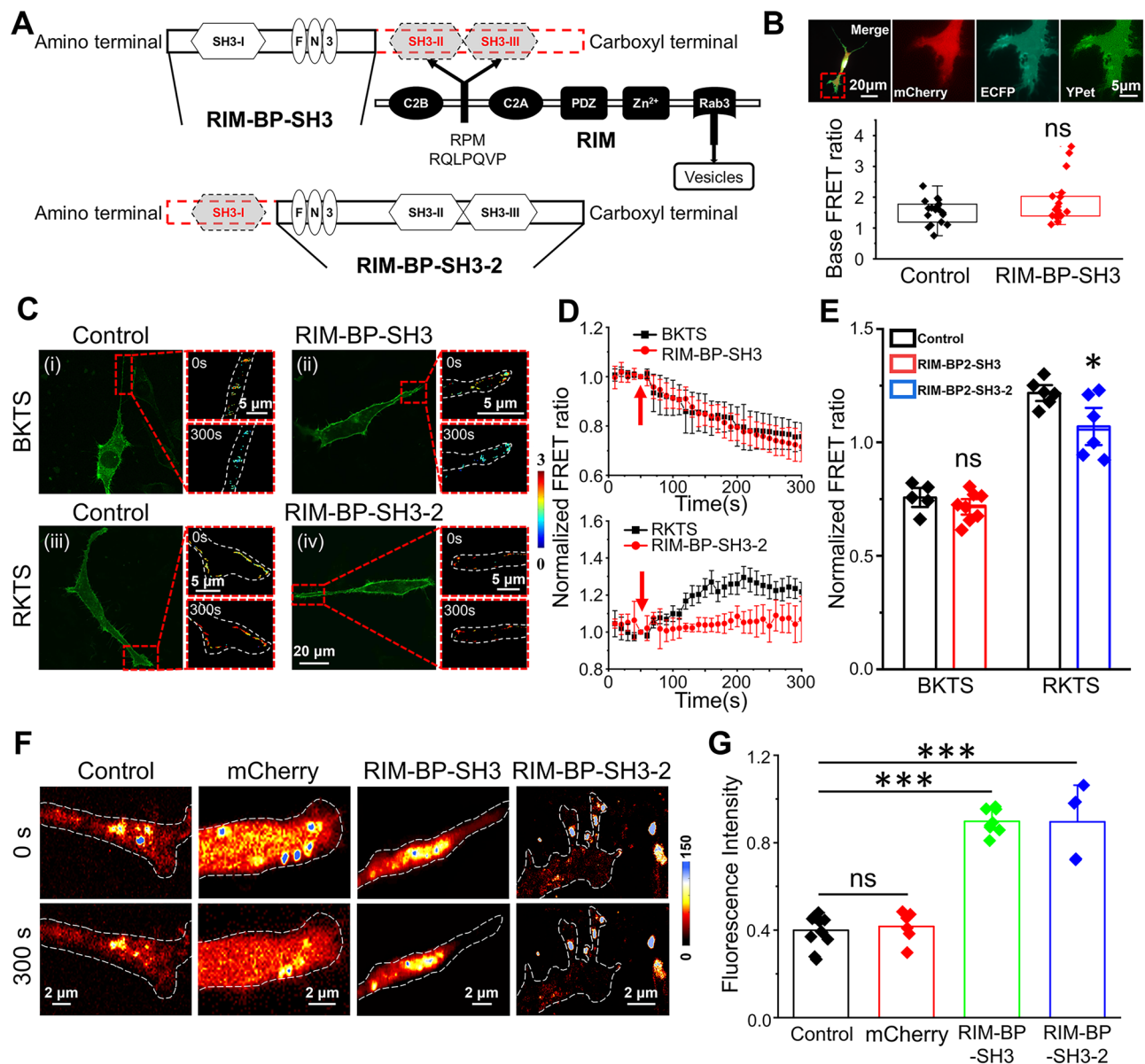
Fig. 6 | The force targeted at the amino terminus of RIM-BP2 leads to the "crane" activity in SH-SY5Y cells. A Schematic of RIM-BP2 mutants. Both mutant probes derived from full-length RIM-BP2. RIM-BP-SH3 probe removed the SH3-II and SH3-III domains (disrupting RIM binding). RIM-BP-SH3-2 probe removed the SH3-I domain (disrupting Bassoon binding). **B** The fluorescent images and FRET ratio baseline analysis of co-expression mCherry-tagged mutant probe with BKTS biosensor in SH-SY5Y cell. mCherry (ex: 580 nm, em: 610 nm), ECFP (ex: 405 nm, em: 488 nm), YPet (ex: 405 nm, em: 530 nm). Control, $n = 18$; RIM-BP-SH3, $n = 19$. **C** The fluorescent images and YPet/ECFP FRET ratio images of BKTS (i, ii) and RKTS (iii, iv) biosensors before (i, iii) and after (ii, iv) the mutation of RIM-BP2.

D Trend of YPet/ECFP FRET ratios for BKTS and RKTS before and after the mutation. Red arrows indicate stimulus onset. BKTS (Control, $n = 5$; RIM-BP-SH3, $n = 8$); RKTS (Control, $n = 6$; RIM-BP-SH3-2, $n = 6$). **E** Comparative analysis of RIM-BP2 "crane" activity before and after mutation. FRET ratio values were measured at 300 s. **F, G** Functional impact of mCherry expression and RIM-BP2 mutation on electrical stimulation-evoked vesicle release. **F** Representative images of FM4-64-labeled vesicle clusters following intracellular expression of mCherry and RIM-BP2 mutants. **G** Quantitative analysis of fluorescence intensity changes. Control, $n = 12$; mCherry, $n = 6$; RIM-BP-SH3, $n = 8$; RIM-BP-SH3-2, $n = 5$. Student's t test. *$P < 0.05$, ***$P < 0.001$, ns $P > 0.05$. Data are mean ± SEM.

FRET technology demonstrates remarkable advantages by skillfully converting those mechanical signals and subtle protein conformational changes that are difficult to observe directly into visually detectable fluorescent signals[48]. With the assistance of fluorescent proteins, this technology effectively extends the duration of signal display, enhancing the feasibility of observation[49]. The spring component connecting the two fluorescent proteins requires excellent mechanical properties and linear response characteristics, which are crucial elements for ensuring the stable and reliable operation of biosensors. In this study, we have designed two types of biosensors to address the rapid changes in RIM-BP2 spatial posture during millisecond-scale neurotransmission. The entropy spring employed at the

core exhibits outstanding mechanical performance, with a maximum stress of 315.3 MPa and a maximum strain of 31.8%[50], making it fully suitable for resolving the mechanical stresses generated during axonal terminal vesicle trafficking (less than 300 pN)[51–53]. Furthermore, the stress-strain behavior of this entropy spring exhibits robust linear response characteristics across various application probes, such as focal adhesions (TSMod)[54], E-Cadherin (CadTS)[55], and integrins (MTS)[56]. Given the unique nature of FRET technology, the normalization method used in this study allowed us to focus on the changes in the FRET ratio across various stimulation conditions, effectively mitigating the errors introduced by differences in baseline among individual cells. The K-means image processing method, helped us

accurately extract the changes in FRET ratio from non-responsive regions with constant FRET ratio. Compared with other methods, such as image processing[57,58] or nuclear magnetic resonance spectroscopy[59], these FRET biosensors enable real-time monitoring in living cells without any effects on the subsequent action potential-induced vesicle release process.

The RIM-BP2 "crane" activity is essentially a stress-induced alteration. Cytoskeleton is one of the most important components in maintaining the stress environment in cells. In neurons, the microfilaments in the pre-synaptic form a meshwork structure[27] and serve as a scaffold for Synapto-physin and Bassoon protein[60,61]. An earlier study discovered a brief rise in the miniature excitatory postsynaptic current following the inhibition of actin polymerization with latrunculin A, suggesting that actin prevents vesicle fusion in the active zone by acting as a physical barrier or tether[60,62]. However, further studies have reached the opposite results. Utilizing CytoD to disrupt actin would damage the recovery of the vesicle pool[63], prevent the recycling of vesicles and alter synaptic activity[64].

This study disrupted actin-mediated force transmission functionality and employed the FM4-64 dye for precise monitoring of vesicle movement under electrical stimulation conditions. FM4-64, being a lipophilic dye, has gained widespread application due to its excellent photostability and membrane-selective properties in detecting vesicle release in various secretory cells[65,66]. The results obtained refine the second theory. Micro-filaments enriched in the presynaptic region transmit power to the vesicle via RIM-BP2, which drives the vesicle toward the presynaptic membrane. The loss of this stress transduction is also accompanied by the disappearance of vesicle release.

However, another cytoskeletal component, the microtubule, is not involved in this process. After the disruption of the microtubule, no change in the "crane" rotation was observed. In neurons, microtubulin can directly bind to the presynaptic proteins synapsin I, synaptotagmin I, and α-synuclein[67–69] to help vesicle aggregation and transport. In addition, microtubules can also regulate the distribution of mitochondria to ensure sufficient energy supply[70–72]. At the same time, although the quantity of vesicle release was not impacted, the rate characteristics were visibly different in the current study. This time lag should be attributed to the active depolymerization[73] and random reassembly of microfilaments after microtubule disruption[74]. This leads to an increasing rate of vesicle release over a certain period of time. Similarly, Babu[75] discovered that the rapid vesicle release process remained unaltered after disrupting the microtubule structure, but the release rate still decreased after prolonged stimulation. It suggests that microtubules might only involve in vesicle transport from the distal reserve pool to the presynaptic membrane[76],

but are not associated with the newly identified mechanotransduction pathway of "the last mile".

In vivo, dynamic changes in membrane tension caused by endocytosis, exocytosis, hydrostatic pressure difference, or cell adhesion[77], usually play a role in stress signal transduction[78]. Membrane tension is usually regulated by membrane fluidity and can lead to further deterioration of neurological diseases such as Alzheimer's disease[79]. Membrane tension and membrane fluidity are usually associated with the expansion of fusion pores of fused vesicles[80,81]. This variation in static membrane tension observed in this study due to the resistance to membrane flow, which comes from the interactions between the plasma membrane and adjacent layers of the underlying cytoskeleton[82–84]. Additionally, as the cell membrane is directly connected to the cytoskeleton, the stretching of the membrane will disrupt its interaction with the cytoskeleton[85], leading to the active rearrangement of the cyto-skeleton to reduce excessive membrane tension, thus protecting the cell from membrane consequences[86–88]. Therefore, it can be speculated that the cell membrane tension affects RIM-BP2 "crane" activity by altering microfila-ment tension.

Based on the performance of the two mutant biosensors, the amino terminus and carboxy terminus of RIM-BP2 serve to transmit microfila-ment stress and traction vesicles, respectively. Although no evidence shows a direct link between actin and RIM-BP2, there is an indirect connection via Bassoon[89]. Therefore, it is reasonable to believe that the Bassoon may transfers the stress from the microfilament to the RIM-BP2. While the FNIII domain in the middle of the two serves as a link between them. It can be connected to the BK potassium channel on the presynaptic membrane to ensure the localization of RIM-BP2 in the active zone[30]. Therefore, this domain may acts as a "fulcrum". Moreover, the neuronal vesicle release activity is a multi-structural complex movement on the nanoscale that also requires some other proteins acting together, such as v-SNARE and t-SNARE[90]. This may explain why destroying the connection of RIM-BP2 to vesicles or directly knocking down RIM-BP2 cannot completely suppress the vesicle release process.

Taken together, our work focused on the vesicle transport from tethering by active zone filaments to docking at the presynaptic membrane, designing molecular spatial distance detection biosensors and proposing a purely mechanical stress regulation mechanism based on RIM-BP2's "crane" activity (Fig. 7). This mechanism, differing from the biochemical factor regulation theory in previous studies, employs a more direct and effective stress dragging approach, offering a new entry point for the vesicle transport theory in this region, and the biosensors we proposed has the potential to serve as an indicator for vesicle release in subsequent studies.
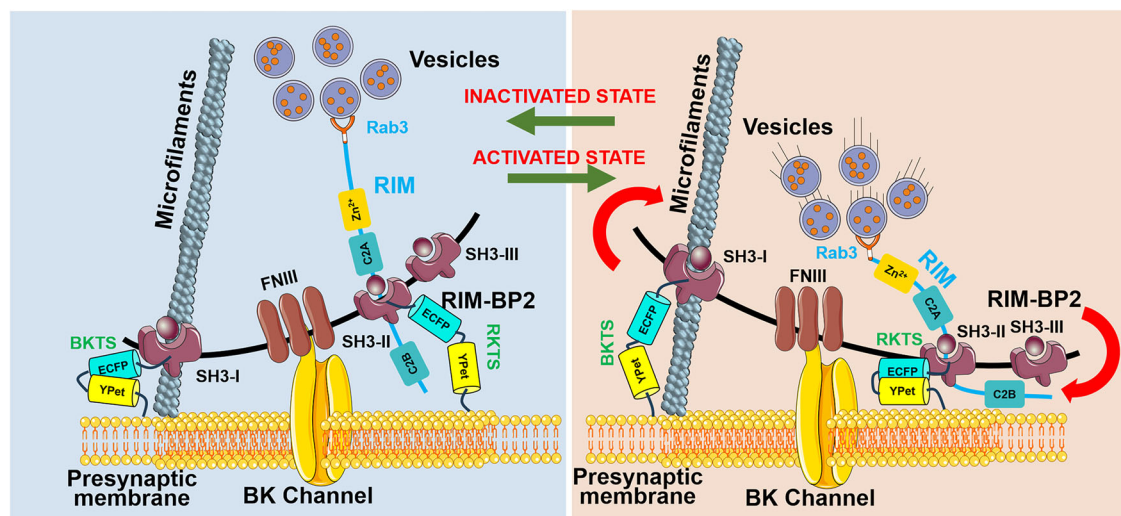

Fig. 7 | The "crane" role of the RIM-BP2 regulates "the last mile" transport of vesicles. The image depicts the relative positions and states of RIM-BP2 and vesicles during inactivated state and activated state. The red curved arrows in the images indicate the rotation direction of both ends of the RIM-BP2 during this process.

Methods

Design of BKTS, RKTS and the control biosensors

Two FRET biosensors, named BKTS and RKTS, which can detect the spatial posture of RIM-BP2, were developed in this study. The stress detecting unit constructed in the center of the biosensor consisted of a YPet/ECFP fluorescent protein pairs for FRET and a molecule spring of which the amino acid sequence was $(GPGGA)_8$ (Fig. 1A)[91]. The one end of BKTS and RKTS biosensors bound to the N- and C-terminus of RIM-BP2, respectively, through different proline-rich PxxP sequences. The BKTS biosensor was linked to the N-terminal of the RIM-BP2 by RTLPSPP derived from the Bassoon[32], while the RKTS was connected to the C-terminal of the RIM-BP2 by RQLPQLP from the RIM[31]. This enabled the specific binding of the biosensors to RIM-BP2. A KRas sequence (KKKKKKKSKTKCVIM) was added to the other end of both BKTS and RKTS biosensors to connect them to phospholipids in the non-lipid raft area of the presynaptic membrane. The control biosensors BTS and RTS both removed the KRas sequence attached to the membrane, leaving the carboxyl terminal of the biosensors free in the cytoplasm. The control biosensor KTS was modified to remove the PxxP sequence that binds to RIM-BP2, allowing it to only be connected to the cell membrane. In addition, two mutant, RIM-BP-SH3 and RIM-BP-SH3-2 based on the entire sequence of RIM-BP2, were also constructed in the study, which were removed the SH3-II/SH3-III domains or SH3-I domain, and carrying the mCherry tag. Both mutants harbor an mCherry fluorescent tag driven by independent promoters to enable real-time visualization and tracking of the mutant cells (Fig. 6A). All biosensors were constructed into pcDNA3.1(+) vector for expression in rat cortical neurons and SH-SY5Y cells, respectively.

Cell culture, transfection and staining

All animal experimentation protocols were approved by the biomedical ethics committee of the Dalian University of Technology and complied with the Guidelines for Treating Experimental Animals issued by the Ministry of Science and Technology of the People's Republic of China. Extensive efforts were made to minimize the number and suffering of the included animals. A total of 30 newborn SD rats were procured from Dalian Medical University Laboratory Animal Center. Dissociated rat cortical neurons from SD rats within 24 h of newborn were cultured in Gibco Neurobasal Medium 1× (Invitrogen, CA, USA) supplemented with Gibco B27 Medium (Invitrogen, CA, USA) and L-glutamine and sustained at 37 °C with 5% CO_2. SH-SY5Y (ATCC, VA, USA) cells were cultured in DMEM supplemented with 10% FBS. The biosensors were transfected with Lipofectamine 3000 reagent (Invitrogen, CA, USA) when cells grew up to 60% of confluency. After that, cells were plated into poly-l-lysine (Sigma, MO, USA) coated confocal dishes, and fluorescent images were taken under stimulation.

In addition, to observe the vesicle release, SH-SY5Y was labeled with FM4-64 (AAT Bioquest, CA, USA) in a static bath for 2 to 5 min, followed by a 10 min wash. During the observation of vesicle release, changes in fluorescence intensity of red spots at the presynaptic membrane after FM4-64 dye staining were analyzed. Red spots from non-neural terminal regions in the same cells were used as controls to avoid the effect of fluorescence quenching or non-specific staining on the results.

High K⁺ solution stimulation and electrical stimulation

High K⁺ solution with the following composition (mM): NaCl, 7.5; KCl, 120; $NaHCO_3$, 25; Myo-Inositol, 3; Na-Pyruvate, 2; NaH_2PO_4, 1.25; Glucose, 25; Ascorbic acid, 0.4; $CaCl_2$, 2 and $MgCl_2$, 1[92] was added dropwise onto cells to induce the action potential. Electrical stimulation was performed using bipolar platinum-iridium alloy electrodes[93] (electrodes diameter of 10 μm and spacing of 50 μm) with a functional signal generator (33250 A, Keysight, CA, USA) and a manual 3D micro-manipulator (FPMAR-HS6, Marzhauser, German). Using the 3D micro-manipulator under a microscope, the bipolar electrode is adjusted to the same horizontal plane as the cell. A square wave electrical signal with a frequency of 10 Hz and a duty cycle of 20% is applied to the middle region of the bipolar electrode. The field strength is set to 5 mV/mm, which is similar to the endogenous electric field of 2.5–5.0 mV/mm recorded in the mammalian brain[94,95].

Microscope image acquisition

The confocal imaging was performed with a laser scanning microscope (IX81-FV1000, Olympus, Japan) with a 100× oil-immersion objective lens. The excitation was from an FV-LD laser at 405 nm, and the emission from ECFP were collected by a detector at 480 ± 15 nm, and YPet at 535 ± 12 nm. The excitation wavelength of mCherry was set to 580 nm and the emission wavelength was 610 ± 10 nm. FM4-64 was excited with a KS3 laser at 558 nm, and its emission was collected using a META detector at 715 ± 35 nm. The multi-channel single-group image was taken for 2.8 s with a shooting interval of 10 s. Five sequential images before the stimulation were taken as the baseline.

Image analysis

The software package used to analyze the spatial posture changing of RIM-BP2 based on Matlab (Version r2019b, MathWorks, MA, USA) contained three sections: pretreatment, cluster, and ratio calculation. First, the background of each image was set as the mean value of the fluorescence intensity from four corners and subtracted to avoid disturbance of the background. The cell body was detected according to the ECFP image by a segmentation algorithm combined with Otsu's method with an adaptive detection threshold. The global threshold was renewed automatically to adapt to the intensity changes in ECFP images. The second section identified the regions with FRET ratio changes by K-means[96] clustering after enhancing the images with a high-pass filter. This is due to the fact that the BKTS/RKTS biosensors employ the KRas sequence as a membrane anchoring domain, which results in full coverage of the membrane signal. To circumvent the issue of signal overabundance, we employ K-means clustering analysis to distinguish between stimulus-responsive and non-responsive regions, thereby extracting the spatial dynamics of the target protein. Furthermore, we also utilize K-means clustering analysis to extract enriched regions from immunofluorescence images and compare them with stimulus-responsive regions in FRET ratio images. Finally, The FRET ratio FRET ratio was considered the FRET index and calculated as Eq. 1 to measure the energy transfer efficiency[97]:

$$\text{FRET ratio} = \frac{E_{transfer}}{E_{total}} \quad (1)$$

Here $E_{transfer}$ was the energy transferred from ECFP to Ypet that was the emission energy of Ypet detected upon the excitation of ECFP. E_{total} was the energy of ECFP, calculated as the sum of the emission energy of ECFP and YPet.

Fluorescence full wavelength scanning

Emission spectra were taken with a Fluorescence Spectrophotometer (Infinite E Plex, Tecan, Switzerland) at room temperature in a quartz cuvette. For measurements, the emission slit resolution was 5 nm. The photomultiplier tube voltage was set at 950 V, and the scan speed was set at 240 nm/min. The emission scan for FRET fluorescent proteins was measured between 420 to 880 nm, and the excitation filter was set to 410 nm. The emission scan for the mixture of FRET fluorescent proteins with FM4-64 was measured between 600 to 880 nm, and the excitation filter was set to 558 nm. Four measurements were taken for each sample, which was repeated at least three times, and the background (air or H_2O) was subtracted from the average.

Statistics and reproducibility

Data were expressed as the mean ± SEM, where n represents the number of cells studied. All FRET ratio (YPet/ECFP) data were normalized by their basal level in the same cell. All statistical analyses of differences between groups were tested by SPSS (Version 26.0, IBM, NY, USA) for unpaired, two-tailed Student's t Test function, Pearson's chi-squared test, LSD

Variance homogeneity test, and one-way ANOVA, respectively followed by Turkey's test. Significant differences were determined by *P*-value. Significance levels are denoted as *P < 0.05, **P < 0.01, ***P < 0.001, ns for *P* > 0.05. For all statistical analysis, data were collected from at least three individual replicates with exact sample numbers indicated in figure legends.

Reporting summary

Further information on research design is available in the Nature Portfolio Reporting Summary linked to this article.

Data availability

Nucleotide sequence for BKTS and RKTS have been deposited in GenBank under the accession numbers PX094062 and PX094063, respectively. Numerical source data for all figures and graphs are provided as a Supplementary Data 1. All other data are available from the corresponding author on reasonable request.

References

1. Fourriere, L., Cho, E. H. J. & Gleeson, P. A. Segregation of the membrane cargoes, BACE1 and amyloid precursor protein (APP) throughout the Golgi apparatus. *Traffic* **23**, 158–173 (2022).
2. Nabb, A. T., Frank, M. & Bentley, M. Smart motors and cargo steering drive kinesin-mediated selective transport. *Mol. Cell Neurosci.* **103**, 1–6 (2020).
3. Velasco, C. D. et al. Microtubule depolymerization contributes to spontaneous neurotransmitter release in vitro. *Commun. Biol.* **6**, 488 (2023).
4. Yogev, S., Cooper, R., Fetter, R., Horowitz, M. & Shen, K. Microtubule organization determines axonal transport dynamics. *Neuron* **92**, 449–460 (2016).
5. Smolders, S. & Van Broeckhoven, C. Genetic perspective on the synergistic connection between vesicular transport, lysosomal and mitochondrial pathways associated with Parkinson's disease pathogenesis. *Acta Neuropathol. Com.* **8**, 1–28 (2020).
6. Pfeffer, S. R. LRRK2 phosphorylation of Rab GTPases in Parkinson's disease. *FEBS Lett.* **597**, 811–818 (2023).
7. Verstreken, P. et al. Synaptic mitochondria are critical for mobilization of reserve pool vesicles at neuromuscular junctions. *Neuron* **47**, 365–378 (2005).
8. Landgraf, A. D. et al. Exploring covalent bond formation at Tyr-82 for inhibition of Ral GTPase activation. *Chemmedchem* **18**, e202300272 (2023).
9. Grigoryev, P. N., Khisamieva, G. A. & Zefirov, A. L. Septin polymerization slows synaptic vesicle recycling in motor nerve endings. *Acta Nat.* **11**, 54–62 (2019).
10. Nagwaney, S. et al. Macromolecular connections of active zone material to docked synaptic vesicles and presynaptic membrane at neuromuscular junctions of mouse. *J. Comp. Neurol.* **513**, 457–468 (2009).
11. Ruiz, R. et al. Active zones and the readily releasable pool of synaptic vesicles at the neuromuscular junction of the mouse. *J. Neurosci.* **31**, 2000–2008 (2011).
12. Bikkumalla, V. et al. Effects of cholesterol on membrane binding by Synaptotagmin-7 C2 domains. *Biophys. J.* **122**, 506A (2023).
13. Kobbersmed, J. R., Berns, M. M., Ditlevsen, S., Sorensen, J. B. & Walter, A. M. Allosteric stabilization of calcium and phosphoinositide dual binding engages several synaptotagmins in fast exocytosis. *Elife* **11**, e74810 (2022).
14. Zhu, J. et al. Synaptotagmin rings as high-sensitivity regulators of synaptic vesicle docking and fusion. *Proc. Natl. Acad. Sci. USA* **119**, 1–11 (2022).
15. Montenegro-Venegas, C. et al. Bassoon controls synaptic vesicle release via regulation of presynaptic phosphorylation and cAMP. *Embo Rep.* **23**, e53659 (2022).
16. Ferreira, C. B. et al. S327 phosphorylation of the presynaptic protein SEPTIN5 increases in the early stages of neurofibrillary pathology and alters the functionality of SEPTIN5. *Neurobiol. Dis.* **163**, 105603 (2022).
17. Jahn, R. & Fasshauer, D. Molecular machines governing exocytosis of synaptic vesicles. *Nature* **490**, 201–207 (2012).
18. Rebola, N. et al. Distinct nanoscale calcium channel and synaptic vesicle topographies contribute to the diversity of synaptic function. *Neuron* **104**, 693–710 (2019).
19. Pieribone, V. A. et al. Distinct pools of synaptic vesicles in neurotransmitter release. *Nature* **375**, 493–497 (1995).
20. Jung, J. H., Kirk, L. M., Bourne, J. N. & Harris, K. M. Shortened tethering filaments stabilize presynaptic vesicles in support of elevated release probability during LTP in rat hippocampus. *Proc. Natl. Acad. Sci. USA* **118**, e2018653118 (2021).
21. Wu, X. D. et al. Vesicle tethering on the surface of phase-separated active zone condensates. *Mol. Cell* **81**, 13–24 (2021).
22. Brockmann, M. M. et al. A trio of active zone proteins comprised of RIM-BPs, RIMs, and Munc13s governs neurotransmitter release. *Cell Rep.* **32**, 107960 (2020).
23. Liu, C. L., Kershberg, L., Wang, J. X., Schneeberger, S. & Kaeser, P. S. Dopamine secretion is mediated by sparse active zone-like release sites. *Cell* **172**, 706–718 (2018).
24. Cingolani, L. A. & Goda, Y. Actin in action: the interplay between the actin cytoskeleton and synaptic efficacy. *Nat. Rev. Neurosci.* **9**, 344–356 (2008).
25. Jerusalem, A. et al. Electrophysiological-mechanical coupling in the neuronal membrane and its role in ultrasound neuromodulation and general anaesthesia. *Acta Biomater.* **97**, 116–140 (2019).
26. Schneider, S. E. et al. Dynamic biophysical responses of neuronal cell nuclei and cytoskeletal structure following high impulse loading. *Acta Biomater.* **163**, 339–350 (2023).
27. Müller, M., Genç, Ö & Davis, G. W. RIM-binding protein links synaptic homeostasis to the stabilization and replenishment of high release probability vesicles. *Neuron* **85**, 1056–1069 (2015).
28. Müller, M., Liu, K. S. Y., Sigrist, S. J. & Davis, G. W. Rim controls homeostatic plasticity through modulation of the readily-releasable vesicle pool. *J. Neurosci.* **32**, 16574–16585 (2012).
29. Liu, K. S. Y. et al. RIM-binding protein, a central part of the active zone, is essential for neurotransmitter release. *Science* **334**, 1565–1569 (2011).
30. Petzoldt, A. G. et al. RIM-binding protein couples synaptic vesicle recruitment to release sites. *J. Cell Biol.* **219**, e201902059 (2020).
31. Hibino, H. et al. RIM binding proteins (RBPs) couple Rab3-interacting molecules (RIMs) to voltage-gated Ca^{2+} channels. *Neuron* **34**, 411–423 (2002).
32. Davydova, D. et al. Bassoon specifically controls presynaptic P/Q-type Ca^{2+} channels via RIM-binding protein. *Neuron* **82**, 181–194 (2014).
33. Krinner, S., Butola, T., Jung, S. Y., Wichmann, C. & Moser, T. RIM-binding protein 2 promotes a large number of Cav1.3 Ca2+-channels and contributes to fast synaptic vesicle replenishment at hair cell active zones. *Front Cell Neurosci.* **11**, 334 (2017).
34. Wen, P. J. et al. Actin dynamics provides membrane tension to merge fusing vesicles into the plasma membrane. *Nat. Commun.* **7**, 1–14 (2016).
35. Li, W. et al. A membrane-bound biosensor visualizes shear stress-induced inhomogeneous alteration of cell membrane tension. *Iscience* **7**, 180–190 (2018).
36. van Helvert, S., Storm, C. & Friedl, P. Mechanoreciprocity in cell migration. *Nat. Cell Biol.* **20**, 8–20 (2018).

37. Meiring, J. C. M., Shneyer, B. I. & Akhmanova, A. Generation and regulation of microtubule network asymmetry to drive cell polarity. *Curr. Opin. Cell Biol.* **62**, 86–95 (2020).

38. Fregno, I. et al. ER-to-lysosome-associated degradation of proteasome-resistant ATZ polymers occurs via receptor-mediated vesicular transport. *Embo J.* **37**, 1–18 (2018).

39. Park, J. C. et al. Fine-tuning GPCR-mediated neuromodulation by biasing signaling through different G protein subunits. *Mol. Cell* **83**, 2540–2558 (2023).

40. Géraldine, M. et al. DHA enhances the noradrenaline release by SH-SY5Y cells. *Neurochem. Int.* **56**, 94–100 (2010).

41. Goodall, A. R., Danks, K., Walker, J. H., Ball, S. G. & Vaughan, P. F. T. Occurrence of two types of secretory vesicles in the human neuroblastoma SH-SY5Y. *J. Neurochem.* **68**, 1542–1552 (1997).

42. Danks, K. et al. Redistribution of F-actin and large dense-cored vesicles in the human neuroblastoma SH-SY5Y in response to secretagogues and protein kinase Cα activation. *Mol. Brain Res.* **64**, 236–245 (1999).

43. Gómez-Santos, C. et al. Dopamine induces autophagic cell death and α-synuclein increase in human neuroblastoma SH-SY5Y cells. *J. Neurosci. Res.* **73**, 341–350 (2003).

44. Grimm, M. O. W. et al. The impact of capsaicinoids on APP processing in Alzheimer's disease in SH-SY5Y cells. *Sci. Rep. UK* **10**, 9164 (2020).

45. Wisessaowapak, C., Visitnonthachai, D., Watcharasit, P. & Satayavivad, J. Prolonged arsenic exposure increases tau phosphorylation in differentiated SH-SY5Y cells: The contribution of GSK3 and ERK1/2. *Environ. Toxicol. Phar* **84**, 103626 (2021).

46. Nakaso, K., Ito, S. & Nakashima, K. Caffeine activates the PI3K/Akt pathway and prevents apoptotic cell death in a Parkinson's disease model of SH-SY5Y cells. *Neurosci. Lett.* **432**, 146–150 (2008).

47. Miao, J., Jing, J., Shao, Y. X. & Sun, H. C. MicroRNA-138 promotes neuroblastoma SH-SY5Y cell apoptosis by directly targeting DEK in Alzheimer's disease cell model. *Bmc Neurosci.* **21**, 33 (2020).

48. Murai, S. et al. Generation of transgenic mice expressing a FRET biosensor, SMART, that responds to necroptosis. *Commun. Biol.* **5**, 1331 (2022).

49. Lipscombe, D. et al. Imaging of cytosolic Ca^{2+} transients arising from Ca^{2+} stores and Ca^{2+} channels in sympathetic neurons. *Neuron* **1**, 355–365 (1988).

50. Teulé, F. et al. Silkworms transformed with chimeric silkworm/spider silk genes spin composite silk fibers with improved mechanical properties. *Proc. Natl. Acad. Sci. USA* **109**, 923–928 (2012).

51. Kunze, A. et al. Modulating motility of intracellular vesicles in cortical neurons with nanomagnetic forces on-chip. *Lab Chip* **17**, 842–854 (2017).

52. Min, D. et al. Mechanical unzipping and rezipping of a single SNARE complex reveals hysteresis as a force-generating mechanism. *Nat. Commun.* **4**, 1705 (2013).

53. Fuson, K. L., Ma, L., Sutton, R. B. & Oberhauser, A. F. The C2 domains of human synaptotagmin 1 have distinct mechanical properties. *Biophys. J.* **96**, 1083–1090 (2009).

54. Grashoff, C. et al. Measuring mechanical tension across vinculin reveals regulation of focal adhesion dynamics. *Nature* **466**, 263–266 (2010).

55. Lagendijk, A. K. et al. Live imaging molecular changes in junctional tension upon VE-cadherin in zebrafish. *Nat. Commun.* **8**, 1402 (2017).

56. Chang, A. C. et al. Single molecule force measurements in living cells reveal a minimally tensioned integrin state. *Acs Nano* **10**, 10745–10752 (2016).

57. Matsumoto, S. et al. Extraction of protein dynamics information from cryo-EM maps using deep learning. *Nat. Mach. Intell.* **3**, 153–160 (2021).

58. Zhang, S. et al. ProDy 2.0: increased scale and scope after 10 years of protein dynamics modelling with Python. *Bioinformatics* **37**, 3657–3659 (2021).

59. Adamski, W. et al. A unified description of intrinsically disordered protein dynamics under physiological conditions using NMR spectroscopy. *J. Am. Chem. Soc.* **141**, 17817–17829 (2019).

60. Lee, J. S., Ho, W. K. & Lee, S. H. Actin-dependent rapid recruitment of reluctant synaptic vesicles into a fast-releasing vesicle pool. *Proc. Natl. Acad. Sci. USA* **109**, E765–E774 (2012).

61. Sankaranarayanan, S., Atluri, P. P. & Ryan, T. A. J. N. Actin has a molecular scaffolding, not propulsive, role in presynaptic function. *Nat. Neurosci.* **6**, 127–135 (2003).

62. Gentile, J. E., Carrizales, M. G. & Koleske, A. J. Control of synapse structure and function by actin and its regulators. *Cells-Basel* **11**, 603 (2022).

63. Phuyal, S. et al. Mechanical strain stimulates COPII-dependent secretory trafficking via Rac1. *Embo J.* **41**, e110596 (2022).

64. Lavoie-Cardinal, F. et al. Neuronal activity remodels the F-actin based submembrane lattice in dendrites but not axons of hippocampal neurons. *Sci. Rep.* **10**, 11960 (2020).

65. Marie, B. et al. Dap160/intersectin scaffolds the periactive zone to achieve high-fidelity endocytosis and normal synaptic growth. *Neuron* **43**, 207–219 (2004).

66. Sala, C. et al. Regulation of dendritic spine morphology and synaptic function by Shank and Homer. *Neuron* **31**, 115–130 (2001).

67. Baines, A. J. & Bennett, V. Synapsin-I is a microtubule-bundling protein. *Nature* **319**, 145–147 (1986).

68. Mazzetti, S., Calogero, A. M., Pezzoli, G. & Cappelletti, G. Cross-talk between α-synuclein and the microtubule cytoskeleton in neurodegeneration. *Exp. Neurol.* **359**, 114251 (2023).

69. Zocchi, R., Compagnucci, C., Bertini, E. & Sferra, A. Deciphering the tubulin language: molecular determinants and readout mechanisms of the tubulin code in neurons. *Int J. Mol. Sci.* **24**, 1–32 (2023).

70. Cheng, X. T. & Sheng, Z. H. Developmental regulation of microtubule-based trafficking and anchoring of axonal mitochondria in health and diseases. *Dev. Neurobiol.* **81**, 284–299 (2021).

71. Parato, J. & Bartolini, F. The microtubule cytoskeleton at the synapse. *Neurosci. Lett.* **753**, 1–11 (2021).

72. Li, S. A. & Sheng, Z. H. Energy matters: presynaptic metabolism and the maintenance of synaptic transmission. *Nat. Rev. Neurosci.* **23**, 4–22 (2022).

73. Goldyn, A. M., Kaiser, P., Spatz, J. P., Ballestrem, C. & Kemkemer, R. The kinetics of force-induced cell reorganization depend on microtubules and actin. *Cytoskeleton* **67**, 241–250 (2010).

74. Ciocanel, M. V. et al. Simulated actin reorganization mediated by motor proteins. *Plos Comput Biol.* **18**, e1010026 (2022).

75. Babu, L. P. A., Wang, H. Y., Eguchi, K., Guillaud, L. & Takahashi, T. Microtubule and actin differentially regulate synaptic vesicle cycling to maintain high-frequency neurotransmission. *J. Neurosci.* **40**, 131–142 (2020).

76. Pekkurnaz, G. & Wang, X. N. Mitochondrial heterogeneity and homeostasis through the lens of a neuron. *Nat. Metab.* **4**, 802–812 (2022).

77. Wang, G. & Galli, T. Reciprocal link between cell biomechanics and exocytosis. *Traffic* **19**, 741–749 (2018).

78. Schumann, J. Molecular mechanism of cellular membranes for signal transduction. *Membr.-Basel* **12**, 748–755 (2022).

79. Fernández-Pérez, E. J. et al. Effect of cholesterol on membrane fluidity and association of Aβ oligomers and subsequent neuronal damage: A Double-Edged Sword. *Front. aging Neurosci.* **10**, 226 (2018).

80. Kliesch, T. T. et al. Membrane tension increases fusion efficiency of model membranes in the presence of SNAREs. *Sci. Rep.* **7**, 1–13 (2017).

81. Lippert, A. H. et al. Soft polydimethylsiloxane-supported lipid bilayers for studying T cell interactions. *Biophys. J.* **120**, 35–45 (2021).

82. Brochard-Wyart, F., Borghi, N., Cuvelier, D. & Nassoy, P. Hydrodynamic narrowing of tubes extruded from cells. *Proc. Natl. Acad. Sci. USA* **103**, 7660–7663 (2006).

83. Shi, Z., Graber, Z. T., Baumgart, T., Stone, H. A. & Cohen, A. E. Cell Membranes Resist Flow. *Cell* **175**, 1769–1779 (2018).
84. Perez, C. G. et al. Rapid propagation of membrane tension at retinal bipolar neuron presynaptic terminals. *Sci. Adv.* **8**, eabl4411 (2022).
85. Cohen, A. E. & Shi, Z. Do cell membranes flow like honey or jiggle like jello?. *Bioessays* **42**, 1900142 (2020).
86. Pagliari, S. et al. YAP-TEAD1 control of cytoskeleton dynamics and intracellular tension guides human pluripotent stem cell mesoderm specification. *Cell Death Differ.* **28**, 1193–1207 (2021).
87. Titelbaum, M. et al. Ezh2 harnesses the intranuclear actin cytoskeleton to remodel chromatin in differentiating Th cells. *Iscience* **24**, 103093 (2021).
88. Peng, X. J., Huang, Y. X. & Alisafaei, F. Cytoskeleton-mediated alterations of nuclear mechanics by extracellular mechanical signals. *Biophys. J.* **121**, 1–3 (2022).
89. Morales, M., Colicos, M. A. & Goda, Y. Actin-dependent regulation of neurotransmitter release at central synapses. *Neuron* **27**, 539–550 (2000).
90. Mochida, S. Stable and flexible synaptic transmission controlled by the active zone protein interactions. *Int J. Mol. Sci.* **22**, 11775 (2021).
91. Shao, S. et al. A DNA-encoded FRET biosensor for visualizing the tension across paxillin in living cells upon shear stress. *Anal. Sens.* **2**, e202100033 (2022).
92. Ghasemi, Z. et al. Effect of low-frequency electrical stimulation on the high-K-induced neuronal hyperexcitability in rat hippocampal slices. *Neuroscience* **369**, 87–96 (2018).
93. Bie, M. et al. Polysaccharide improves bipolar pulse current-induced microglia cell injury through modulating autophagy. *Cell Transpl.* **24**, 419–428 (2015).
94. Fröhlich, F. & McCormick, D. A. Endogenous electric fields may guide neocortical network activity. *Neuron* **67**, 129–143 (2010).
95. Qiu, C., Shivacharan, R. S., Zhang, M. M. & Durand, D. M. Can neural activity propagate by endogenous electrical field?. *J. Neurosci.* **35**, 15800–15811 (2015).
96. Ahmed, M., Seraj, R. & Islam, S. M. S. The K-means algorithm: a comprehensive survey and performance evaluation. *Electron.-Switz.* **9**, e9081295 (2020).
97. Morimatsu, M., Mekhdjian, A. H., Adhikari, A. S. & Dunn, A. R. Molecular tension sensors report forces generated by single integrin molecules in living cells. *Nano Lett.* **13**, 3985–3989 (2013).

Acknowledgements

Author contributions

T.G. and B.L. designed the study. T.G. wrote the manuscript. T.G., W.L., S.S. and Z.Z. performed the experiments and analyzed the data. N.L., H.Z. and B.L. revised the manuscript. The final version of the manuscript was reviewed and approved by all authors.

Competing interests

The authors declare no competing interests.

Additional information

Supplementary information The online version contains supplementary material available at https://doi.org/10.1038/s42003-025-08747-9.

Correspondence and requests for materials should be addressed to Bo Liu.

Peer review information *Communications Biology* thanks Stephan Sigrist and the other, anonymous, reviewer(s) for their contribution to the peer review of this work. Primary Handling Editor: Benjamin Bessieres. A peer review file is available.

Reprints and permissions information is available at http://www.nature.com/reprints

Publisher's note Springer Nature remains neutral with regard to jurisdictional claims in published maps and institutional affiliations.